Compliant Tracking Control and Force Redistribution for a Portable Cable-Driven Robot

Haining Sun, *Member, IEEE*, Xiaoqiang Tang, and Shuzhi Sam Ge, *Fellow, IEEE*

***Abstract*—This study introduces the development of a portable cable-driven robot with a compliant trajectory tracking method that incorporates real-time and continuous positive force redistribution. Based on the dynamic model of the robot, a rapid-convergence tracking controller exhibiting variable compliance to external disturbances is designed to ensure stable trajectory tracking. A real-time, continuous positive force redistribution process is seamlessly integrated into the tracking controller to ensure that cable forces remain positive and continuous throughout the motion. Low compliance allows the robot to resist external disturbances and maintain accurate trajectory tracking. Conversely, high compliance permits the robot to temporarily sacrifice some tracking accuracy for safety and then resume tracking once the disturbance subsides. Lyapunov stability analysis is utilized to validate the stability of the control system. Experiments are conducted on the designed robot to evaluate the practical applicability of the control method. Results demonstrate the feasibility of the force redistribution without compromising trajectory tracking performance.**

***Index Terms*—Motion control, force redistribution, cable-driven robot**

I. INTRODUCTION

CABLE-Driven robots (CDRs) have emerged as a promising solution for achieving motion and dynamic control within large workspaces in diverse industrial applications, such as construction 3D printing [1], vibration control of large-span flexible wings [2], and façade operations [3]. Various advanced control techniques have been explored for CDRs, including neural network-based control [4], vision-based control [5], synchronization control [6], sliding mode control [7], [8], and reference trajectory shaping methods [9], among others. These technologies have proven effective in ensuring accurate trajectory tracking control. Specifically, Shang *et al.* [6] proposed synchronized controllers to reduce trajectory tracking errors while minimizing synchronization errors between different cables. However, the aforementioned tracking controllers do not reflect the force redistribution. A fundamental characteristic of cables is their ability to withstand tensile forces but not resist compressive forces. This limitation can lead to cable slack in CDRs, causing deviations from desired trajectories and potentially affecting critical operations in industrial applications.

CDRs maintain cable's taut state through either passive or active cable forces. In under-constrained CDRs, equilibrium is achieved by generating passive cable forces, which can result from their own gravity or external forces [10]-[13]. Fully constrained CDRs, on the other hand, feature non-unique solutions for cable forces, allowing active adjustment of cable forces to meet specific constraints. Some studies have utilized the concept of internal forces to maintain cable tension, often by computing the null-space vectors of the transposed Jacobian matrix and integrating them into control inputs [14]-[24]. For instance, Wang *et al.* [14] linearly incorporated null-space vectors into the control input to ensure that cable forces remain within an acceptable range during Schönflies trajectory tracking. A robust PID controller incorporating a corrective term that consists of null-space vectors was designed to maintain bounded tracking errors [15]. Similarly, several trajectory tracking controllers, such as adaptive robust control [16], composite control [17], dual-loop position and force control [18], PD feedback control [19] and vision-based H_∞ position control [20], have utilized internal forces derived from the null-space vector to ensure force constraints are met. However, these studies often neglected the continuity and real-time efficiency of the force distribution. They primarily focused on tracking performance and directly imposing force constraints on control inputs. For example, Kawamura *et al.* [19] focused on improving trajectory tracking performance without documenting the corresponding cable forces. An iterative redundancy distribution algorithm leveraging the null space was discussed for its theoretical advantages in [21], but its real-time applicability requires enhancement. A tension-level index was introduced to improve force distribution and achieve the desired cable forces [22]. However, relying solely on internal forces during trajectory tracking may not always produce continuous cable forces that satisfy the constraints. Simulations in [25] show that there is still significant room for improvement in internal force-based control strategies for reducing trajectory tracking errors.

Recent research has explored geometric methods that leverage null-space vectors to optimize the distribution of

Manuscript received September xx, 2023. This work was supported by the National Natural Science Foundation of China under Grant 51975307 and the Ministry of Education, Singapore, under its Research Centre of Excellence award to the Institute for Functional Intelligent Materials (I-FIM, project No. EDUNC-33-18-279-V12). (Corresponding author: X. Tang and S. S. Ge).

H. Sun is with the State Key Laboratory of Tribology, Department of Mechanical Engineering, Tsinghua University, Beijing, 100084, China and also with the Singapore Institute of Manufacturing Technology, Agency for Science, Technology and Research (A*STAR), Singapore 138634, Republic of Singapore (e-mail: sunhn@simtech.a-star.edu.sg).

X. Tang is with the State Key Laboratory of Tribology, Department of Mechanical Engineering, Tsinghua University, Beijing, 100084, China (e-mail: tang-xq@mail.tsinghua.edu.cn).

S. S. Ge is with the Department of Electrical and Computer Engineering, and Institute for Functional Intelligent Materials, National University of Singapore, Singapore 117583 (e-mail: samge@nus.edu.sg)

Supplemental materials contain a PDF file ("Supplementary Material 1") and a video ("Video.mp4").

cable forces in CDRs [26]-[27]. A force distribution method using convex polygons was developed to improve computational efficiency [26]. However, this approach was tailored explicitly for CDRs with $n + 2$ cables and n degrees of freedom (DOFs). To satisfy the real-time requirement, a tension-distribution calculation method using the hypersphere mapping algorithm was proposed in [27]. It's crucial to note that the complexity of these geometric methods increases with the redundancy (the number of cables minus controllable DOFs). As redundancy increases, the dimensionality of the polyhedron formed by the convex set also increases, leading to longer search times and greater difficulty in determining the optimal solution. When redundancy is limited (usually one or two), geometric methods have proven to be effective, as high redundancy significantly increases computational costs.

To avoid using internal forces, some studies directly integrated the cable force distribution into the framework of controllers. For example, a hyperbolic function-based saturation function was employed to convert original control inputs into positive cable forces [25]. This approach utilized a nonlinear observer to balance discrepancies in cable forces under both unconstrained and constrained scenarios. However, using saturation functions can lead to inconsistencies between the boundary of expected cable forces and the boundary of solved cable forces. To address this limitation, researchers developed model predictive control [28] and nonlinear model predictive control [29] techniques for accurate trajectory tracking and handling force redistribution. These methods determine the optimized cable forces within specified constraints by formulating and minimizing a cost function. These cost functions typically include the tracking error and the 2-norm of the cable forces. Results revealed that changes in the constraint of cable forces directly impacted trajectory tracking performance. This could be attributed to the cost function that couples the tracking error and cable forces together. This coupling led to a trade-off where adjustments in one constraint affected the other, making it difficult for the controller to consistently prioritize tracking errors.

For CDRs, achieving accurate trajectory tracking is not only dependent on effectively distributing cable forces but also handling unpredictable external disturbances such as varying external forces and fluctuations in payloads. These disturbances can impact the stability of the trajectory-tracking process. On one hand, to improve resistance against external disturbances and enhance trajectory tracking, it is desirable for the CDR to have low compliance. On the other hand, in scenarios involving human-robot interaction, higher compliance helps avoid excessive cable forces, allowing the robot to prioritize safety over strict tracking performance. The robot can temporarily sacrifice some tracking accuracy but regain it once disturbances are mitigated. However, previous works in [4], [6]-[9], [12]-[13], [16]-[17], [19]-[24], [27], [29]-[32] have generally overlooked the influence of external disturbances and the compliance of tracking controllers to these disturbances. In previous studies [14], [15], [18], constant external disturbances were replaced by additional payloads and thus were integrated into the tracking controller.

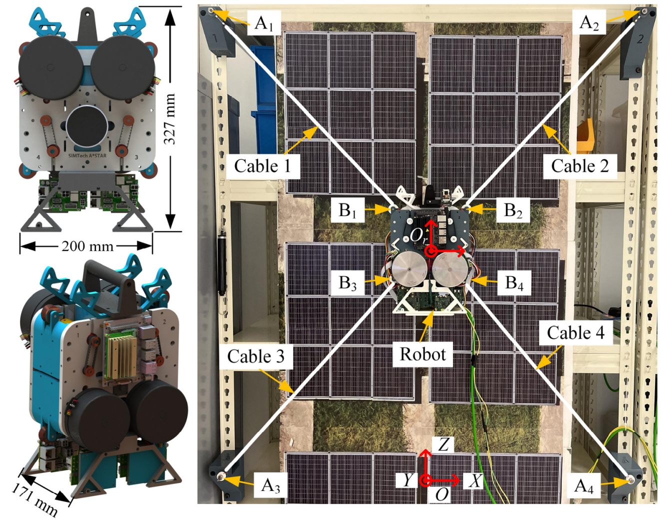

Fig. 1. The designed portable cable-driven robot.

In [33], the designed compliance control mainly focused on maintaining low compliance to ensure accurate trajectory tracking under heavy loads, without validating its capability to exhibit higher compliance when encountering external disturbances. Similarly, the impedance control proposed in [34] achieved satisfying position and force tracking but did not verify the robot's ability to exhibit high compliance under external forces. Furthermore, the calculation of cable forces in [34] relied on the null-space vectors of the Jacobian matrix. To allow for deviations from the predetermined trajectory under external forces, Barroso *et al.* [35] utilized springs to provide high compliance for the CDR, offering a safe environment for human-robot interaction. Recognizing these gaps, this work aims to address the challenges of tracking control in CDRs, particularly the need for adjustable compliance in response to external disturbances.

The contributions of this study are as follows:

1) The designed auxiliary tracking controller eliminates chattering in the control input through integral processing. It features adjustable compliance against external disturbances, allowing a trade-off between trajectory tracking accuracy and compliance. Low compliance enhances the robot's resistance to disturbances, thereby ensuring tracking accuracy, while high compliance allows the robot to temporarily sacrifice trajectory tracking accuracy to mitigate the risk of significant cable forces.
2) A real-time force redistribution algorithm is introduced to ensure that cable forces remain continuous, thereby avoiding sudden discrete jumps. The cable forces are redistributed within given constraints without affecting the stability of the control system. This force redistribution algorithm does not compromise trajectory tracking performance and is seamlessly integrated with the auxiliary tracking control.
3) Unlike the CDRs in [9-35], our robot body integrates mechanical and electronic components for portability and rapid deployment, and is designed to function as an independent and motion-capable unit. Weighing 7.8 kg and measuring 327 × 200 × 171 mm, it is easy for one person

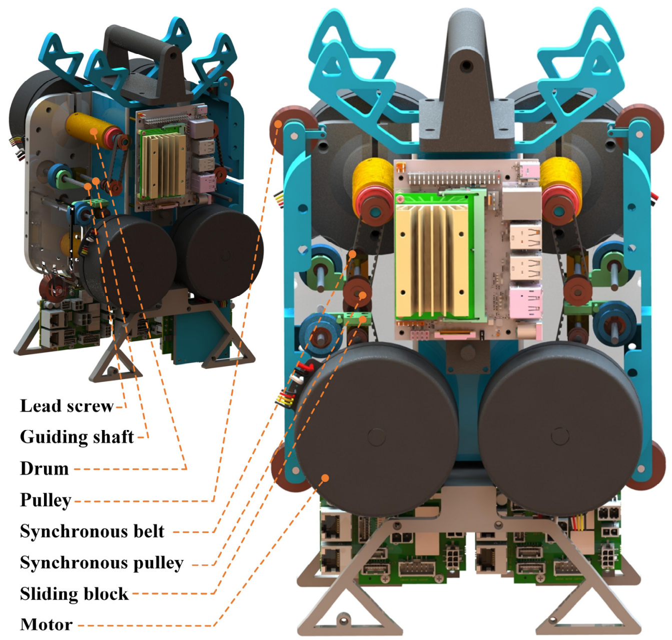

Fig. 2. CAD model of the robot.

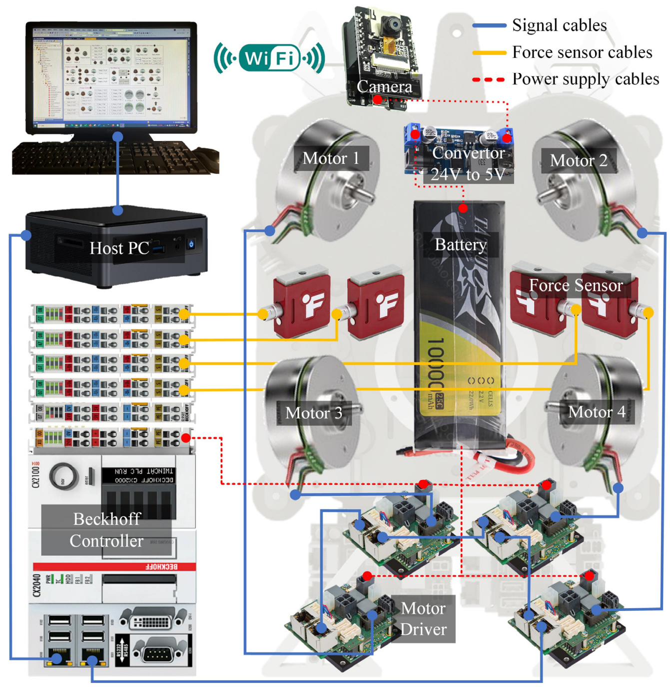

Fig. 3. Diagram of electronic components of the robot.

to set up and deploy. Requiring only four simple anchors from environments, it provides three controllable degrees of freedom. Its workspace can be rapidly reconfigured within 94 s, transitioning from one workspace to another, allowing rapid restoration of operations (see video).

4) Experiments are conducted on the developed portable CDR (see Fig. 1 and supplementary video). The results verify the robot's ability to resist external disturbances and maintain accurate trajectory tracking at low compliance. Under high compliance, even with a deviation of up to 65.9 mm, the robot can still maintain stable trajectory tracking and return to the predetermined trajectory once the disturbances are over.

The subsequent sections of this paper are structured as follows: Section II describes the hardware components of the robot. Section III introduces the robot's dynamic model. Section IV details the controller design. In Section V, experiments are conducted on the developed robot to validate the practical applicability of the control method. Section VI concludes the work.

II. Robot Components Overview

To achieve portability, quick deployment, and rapid reconfiguration of the workspace for the robot, we integrated the mechanical and electronic components into the robot's main body. The entire unit weighs only 7.8 kg and has a compact size of 327 mm × 200 mm × 171 mm, making it easy for one person to carry. Fig. 2 depicts the mechanical structure of the robot. Each cable is wound in a spiral pattern around a 25 mm-diameter drum, passes through two pulleys, and then anchors to the simple anchors within the environment. To ensure neat alignment of cables along the drum surface during winding and unwinding operations, an internal cable winding mechanism has been integrated into the robot. The mechanism consists of synchronized pulleys, timing belts, lead screws and guiding shafts. The transmission ratio of the synchronous belts is 1:1. One pulley is fixed directly to the motor shaft, while the other is connected to the lead screw. The guiding shaft, together with the sliding block, converts the rotation of the lead screw into linear motion along the axis of the drum. The pitch of the helix on the lead screw and drum is 1 mm.

In addition to the aforementioned mechanical structures, the robot also integrates essential electronic components, including motors, motor drives, force sensors, a controller, and a camera, as shown in Fig. 3. The corresponding technological specifications are:

1) Controller: Beckhoff PLC with Intel® Core™ i7 2715QE 2.1 GHz processor (4 cores), power supply unit, EL9505 5V DC power supply terminal, and EL3356 EtherCAT terminals. Motor and drive: Four Maxon Brushless EC 90 flat motors (260 W, nominal speed: 1670 rpm, nominal torque: 964 mNm) with Hall sensors and MILE 2-channel encoder (2048 counts per turn). Four Maxon EPOS4 Compact 50/15 EtherCAT drives.
2) Sensors: Four Futek LSB205 load cells.
3) Battery: 22.2 V 6s Lipo battery with 10,000 mAh for the Beckhoff controller, motor drives, and force sensors.
4) Others: Inter NUC for programming and user interface.

The robot requires only four simple external anchor points, and the positions of these anchor points can be changed quickly. Its workspace can be rapidly reconfigured within 94 s, transitioning from one workspace to another, allowing rapid restoration of operations (kindly see the supplementary video). Fig. 4 shows four different workspaces, each with a distinct shape and size. A_1–A_4 represents four anchor points. When anchor point A_4 moves down, the workspace shifts from the rectangular shape in Fig. 4(a) to the trapezoidal shape in Fig. 4(b). Subsequently, as A_4 moves to the right, the workspace expands into another trapezoidal shape, as shown in Fig. 4(c).

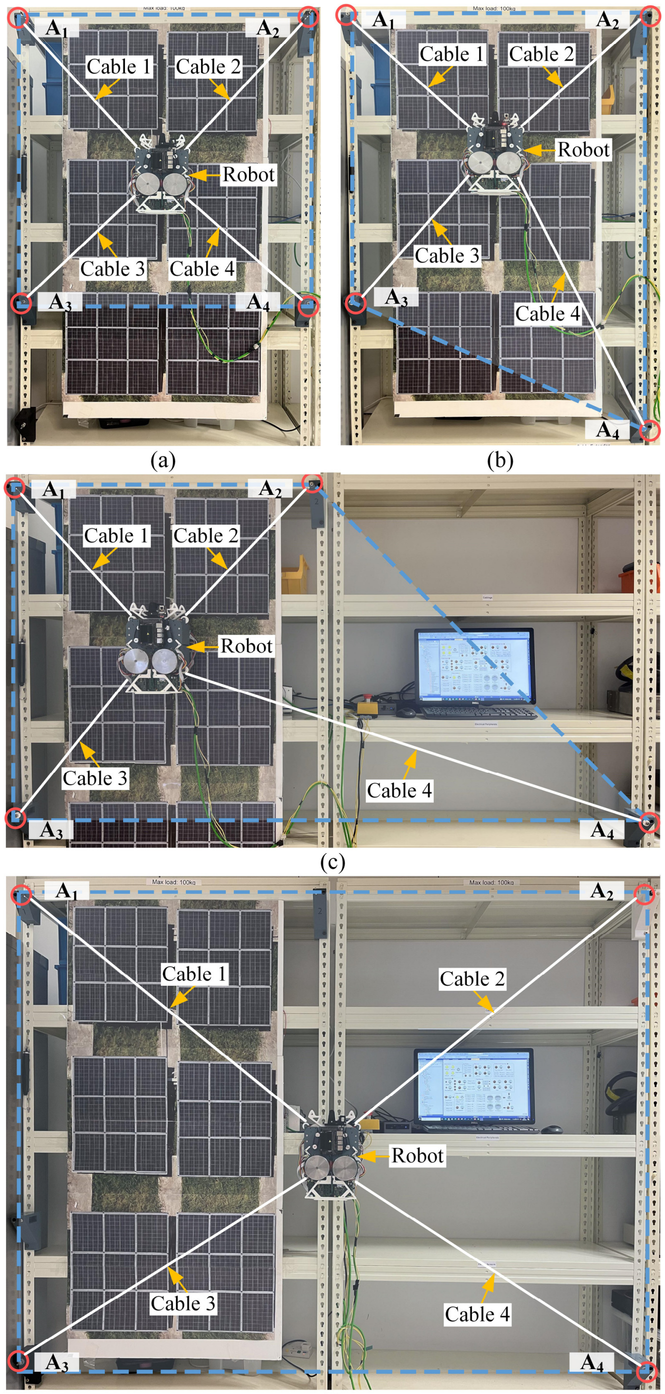

Fig. 4. Reconfiguration of the robot's workspace. (a) – (d) represents four different workspaces.

Finally, the workspace is further enlarged by moving A_2 rightward as well as A_3 and A_4 downward (see Fig. 4(d)).

III. Dynamic Model

This portion describes the dynamic model of the portable robot, including an unknown disturbance term. The model is simplified by assuming that the cables connecting the robot's body (B_i) to the environmental anchor points A_i have negligible mass. As shown in Fig. 1, the reference coordinate frame $\{O\}$ is positioned on the ground, while the moving coordinate frame $\{O_r\}$ is placed at the robot's center of mass. Based on the vector loop equation, the robot's kinematic model can be formulated as:

$$\boldsymbol{p} = \boldsymbol{a}_i - \boldsymbol{l}_i - {}^{O}\boldsymbol{R}_{O_r}\boldsymbol{b}_i \;\; (i = 1,2,\ldots,m). \tag{1}$$

where the vector $\boldsymbol{l}_i$ originates from B_i and terminates at A_i, $\boldsymbol{a}_i$ denotes the location of A_i within $\{O\}$, $\boldsymbol{p}$ is the location of $\{O_r\}$ in $\{O\}$, ${}^{O}\boldsymbol{R}_{O_r}$ is the rotation matrix, $\boldsymbol{b}_i$ denotes the location of B_i within $\{O_r\}$, and m denotes the total count of cables. The dynamic model with unknown disturbance $\boldsymbol{T}_d$ is expressed by:

$$\begin{bmatrix} m_r\boldsymbol{I}_{3\times3} & \boldsymbol{0}_{3\times3} \\ \boldsymbol{0}_{3\times3} & \boldsymbol{I}_r \end{bmatrix}\begin{bmatrix} \ddot{\boldsymbol{p}} \\ \dot{\boldsymbol{\omega}} \end{bmatrix} + \begin{bmatrix} \boldsymbol{0}_{3\times1} \\ \boldsymbol{\omega}\times\boldsymbol{I}_r\boldsymbol{\omega} \end{bmatrix} + \begin{bmatrix} m_r\boldsymbol{g} \\ \boldsymbol{0}_{3\times1} \end{bmatrix} + \boldsymbol{T}_d = -\boldsymbol{J}_{\omega}{}^{T}\boldsymbol{u}. \tag{2}$$

where m_r and $\boldsymbol{I}_r$ respectively symbolize the mass and inertia matrix of the whole robot body. $\boldsymbol{\omega} = \boldsymbol{E}\dot{\boldsymbol{\theta}}$ denotes the robot's angular velocity. $\boldsymbol{\theta} = [\alpha,\beta,\gamma]^T$ is the vector of Euler angles. Jacobian matrix $\boldsymbol{J}_{\omega}$ is expressed by:

$$\boldsymbol{J}_{\omega} = \begin{bmatrix} \boldsymbol{r}_1 & \boldsymbol{r}_2 & \cdots & \boldsymbol{r}_m \\ {}^{O}\boldsymbol{R}_{O_r}\boldsymbol{b}_1\times\boldsymbol{r}_1 & {}^{O}\boldsymbol{R}_{O_r}\boldsymbol{b}_2\times\boldsymbol{r}_2 & \cdots & {}^{O}\boldsymbol{R}_{O_r}\boldsymbol{b}_m\times\boldsymbol{r}_m \end{bmatrix}^T. \tag{3}$$

where the unit vector $\boldsymbol{r}_i$ along the i-th cable is expressed as $\boldsymbol{r}_i = \boldsymbol{l}_i / l_i$. The cable length l_i is expressed by:

$$l_i = \sqrt{\left[\boldsymbol{a}_i - \boldsymbol{p} - {}^{O}\boldsymbol{R}_{O_r}\boldsymbol{b}_i\right]^T \cdot \left[\boldsymbol{a}_i - \boldsymbol{p} - {}^{O}\boldsymbol{R}_{O_r}\boldsymbol{b}_i\right]}. \tag{4}$$

Let $c(\cdot) = \cos(\cdot)$ and $s(\cdot) = \sin(\cdot)$, then the dynamic model (2) can be rewritten as:

$$\boldsymbol{M}(\boldsymbol{x})\ddot{\boldsymbol{x}} + \boldsymbol{C}(\boldsymbol{x},\dot{\boldsymbol{x}})\dot{\boldsymbol{x}} + \boldsymbol{G}(\boldsymbol{x}) + \boldsymbol{T}_d = -\boldsymbol{J}^T\boldsymbol{u} \tag{5}$$

where $\boldsymbol{x} = [\boldsymbol{p},\boldsymbol{\theta}]^T = [x_p, y_p, z_p, \alpha, \beta, \gamma]^T$ represents the portable robot's posture in the workspace. $\boldsymbol{u} = [u_1,\ldots,u_m]^T$ is the cable force vector. $\boldsymbol{G}(\boldsymbol{x}) = [m_r\boldsymbol{g},\ \boldsymbol{0}_{3\times1}]^T$ is the gravity wrench, $\boldsymbol{g} = [0,\ 0,\ -9.8]^T$ m/s^2. The new Jacobian matrix $\boldsymbol{J}$ is expressed by:

$$\boldsymbol{J} = \boldsymbol{J}_{\omega}\begin{bmatrix} \boldsymbol{I}_{3\times3} & \boldsymbol{0}_{3\times3} \\ \boldsymbol{0}_{3\times3} & \boldsymbol{E} \end{bmatrix} \tag{6}$$

The inertia matrix $\boldsymbol{M}(\boldsymbol{x})$ and the Coriolis and centrifugal matrix $\boldsymbol{C}(\boldsymbol{x},\dot{\boldsymbol{x}})$ are expressed by:

$$\boldsymbol{M}(\boldsymbol{x}) = \begin{bmatrix} m_r\boldsymbol{I}_{3\times3} & \boldsymbol{0}_{3\times3} \\ \boldsymbol{0}_{3\times3} & \boldsymbol{E}^T\boldsymbol{I}_r\boldsymbol{E} \end{bmatrix} \tag{7}$$

$$\boldsymbol{C}(\boldsymbol{x},\dot{\boldsymbol{x}}) = \begin{bmatrix} \boldsymbol{0}_{3\times3} & \boldsymbol{0}_{3\times3} \\ \boldsymbol{0}_{3\times3} & \boldsymbol{E}^T\boldsymbol{E}_{\theta}\boldsymbol{I}_r\boldsymbol{E} + \boldsymbol{E}^T\boldsymbol{I}_r\dot{\boldsymbol{E}} \end{bmatrix} \tag{8}$$

where

$$\boldsymbol{E} = \begin{bmatrix} c\beta c\gamma & -s\gamma & 0 \\ c\beta s\gamma & c\gamma & 0 \\ -s\beta & 0 & 1 \end{bmatrix} \tag{9}$$

$$\boldsymbol{E}_{\theta} = \begin{bmatrix} 0 & s\beta\dot{\alpha} - \dot{\gamma} & c\beta s\gamma\dot{\alpha} + c\gamma\dot{\beta} \\ -s\beta\dot{\alpha} + \dot{\gamma} & 0 & -c\beta c\gamma\dot{\alpha} + s\gamma\dot{\beta} \\ -c\beta s\gamma\dot{\alpha} - c\gamma\dot{\beta} & c\beta c\gamma\dot{\alpha} - s\gamma\dot{\beta} & 0 \end{bmatrix} \tag{10}$$

IV. Controller Design

A. Observer

Assuming the prescribed target trajectory is $\boldsymbol{x}_d = [x_d, y_d, z_d, \alpha_d, \beta_d, \gamma_d]^T$, the tracking error, denoted as $\boldsymbol{e}$, is expressed as:

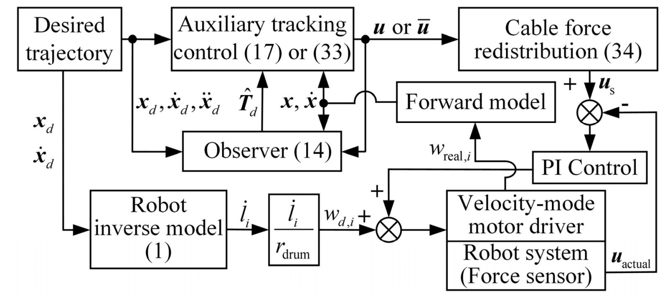

Fig. 5. Control block diagram of the controller.

$$\boldsymbol{e} = \boldsymbol{x} - \boldsymbol{x}_d. \tag{11}$$

The acceleration tracking error could be obtained by substituting (11) into the dynamic model (5):

$$\begin{aligned}\ddot{\boldsymbol{e}} = \ddot{\boldsymbol{x}} - \ddot{\boldsymbol{x}}_d &= \boldsymbol{M}^{-1}(\boldsymbol{x})\big(-\boldsymbol{J}^T\boldsymbol{u} - \boldsymbol{C}(\boldsymbol{x},\dot{\boldsymbol{x}})\dot{\boldsymbol{x}} \\ &\quad -\boldsymbol{G}(\boldsymbol{x}) - \boldsymbol{T}_d\big) - \ddot{\boldsymbol{x}}_d.\end{aligned} \tag{12}$$

where $\boldsymbol{M}^{-1}(x)$ is the inverse matrix of $\boldsymbol{M}(x)$. Let $\dot{\boldsymbol{e}} = \boldsymbol{x}_{z1}$ be one state of the tracking error system (12) and let an extended state $\boldsymbol{x}_{z2}$ represent the external disturbance, then it's feasible to formulate the following state equation:

$$\begin{cases}\dot{\boldsymbol{x}}_{z1} = \boldsymbol{x}_{z2} + \boldsymbol{M}^{-1}(\boldsymbol{x})\big(-\boldsymbol{J}^T\boldsymbol{u} - \boldsymbol{C}(\boldsymbol{x},\dot{\boldsymbol{x}})\dot{\boldsymbol{x}} - \boldsymbol{G}(\boldsymbol{x})\big) - \ddot{\boldsymbol{x}}_d \\ \dot{\boldsymbol{x}}_{z2} = -\boldsymbol{M}^{-1}(\boldsymbol{x})\dot{\boldsymbol{T}}_d\end{cases}. \tag{13}$$

Based on (13), the designed observer is:

$$\begin{cases}\dot{z}_1 = z_2 + \boldsymbol{M}^{-1}(\boldsymbol{x})\big(-\boldsymbol{J}^T\boldsymbol{u} - \boldsymbol{C}(\boldsymbol{x},\dot{\boldsymbol{x}})\dot{\boldsymbol{x}} - \boldsymbol{G}(\boldsymbol{x})\big) \\ \quad -\boldsymbol{\beta}_1(z_1 - \dot{\boldsymbol{e}}) - \ddot{\boldsymbol{x}}_{\mathrm{d}} \\ \dot{z}_2 = -\boldsymbol{\beta}_2(z_1 - \dot{\boldsymbol{e}}) \\ z_2 = -\boldsymbol{M}^{-1}(\boldsymbol{x})\hat{\boldsymbol{T}}_d\end{cases}. \tag{14}$$

where z_1 and z_2 are two states of the observer, which are used to approximate the error $\dot{\boldsymbol{e}}$ and extended state $\boldsymbol{x}_{z2}$, respectively. $\hat{\boldsymbol{T}}_d$ represents the estimated value of the external disturbance $\boldsymbol{T}_d$. Then, $\hat{\boldsymbol{T}}_d$ will be integrated into the auxiliary trajectory tracking control. Two diagonal gain matrixes $\boldsymbol{\beta}_1$ = diag([β_{11},..., β_{16}]) and $\boldsymbol{\beta}_2$ = diag([β_{21},..., β_{26}]) contain positive elements. Regarding the external disturbance, we make the following assumption:

Assumption 1: The external disturbance $\boldsymbol{T}_d = [T_{d1}, T_{d2}, T_{d3}, T_{d4}, T_{d5}, T_{d6}]^T$ is slow-varying and satisfies the following conditions:

$$\begin{aligned}&\lim_{t\to\infty}\dot{T}_{d1} = 0, \quad \lim_{t\to\infty}\dot{T}_{d2} = 0, \quad \lim_{t\to\infty}\dot{T}_{d3} = 0 \\ &\lim_{t\to\infty}\dot{T}_{d4} = 0, \quad \lim_{t\to\infty}\dot{T}_{d5} = 0, \quad \lim_{t\to\infty}\dot{T}_{d6} = 0\end{aligned} \tag{15}$$

Lemma 1: The observer in (14) can ensure that errors $\boldsymbol{e}_{z1}$ and $\boldsymbol{e}_{z2}$ ultimately converge to zero:

$$\lim_{t\to\infty}\boldsymbol{e}_{z1}(t) = \boldsymbol{0}, \ \lim_{t\to\infty}\boldsymbol{e}_{z2}(t) = \boldsymbol{0} \tag{16}$$

Proof: Due to page limitations, we have placed the proof of *Lemma 1* in a supplementary PDF file ("Supplementary Material 1.pdf"). Kindly refer to it for further information.

B. Auxiliary Tracking Control

The entire control block diagram is shown in Fig. 5. The auxiliary tracking control incorporates inputs such as the target trajectory, $\boldsymbol{x}_d$, $\dot{\boldsymbol{x}}_d$, and $\ddot{\boldsymbol{x}}_{\mathrm{d}}$, the actual posture feedback $\boldsymbol{x}$ and $\dot{\boldsymbol{x}}$, as well as the estimated disturbance $\hat{\boldsymbol{T}}_d$ derived from the designed observer in (14). The inputs of the observer include $\boldsymbol{x}_d$, $\dot{\boldsymbol{x}}_d$, $\ddot{\boldsymbol{x}}_{\mathrm{d}}$, $\boldsymbol{x}$, $\dot{\boldsymbol{x}}$, and the output of the auxiliary tracking control. The force redistribution process is then employed to complete the secondary distribution of cable forces, ensuring that the optimized cable forces satisfy the constraint conditions and the specified objective function. As the output of the auxiliary tracking control, the cable force vector $\boldsymbol{u}$ is designed as follows:

$$\begin{aligned}\boldsymbol{u} &= \left(\boldsymbol{J}^T\right)^{\dagger}\boldsymbol{M}(\boldsymbol{x})\left(\boldsymbol{H}\left(\boldsymbol{1}_{6\times 1} + \frac{g}{h}\boldsymbol{\alpha}\boldsymbol{e}^{\frac{g}{h}-1}\right)\right) \\ &\quad -\left(\boldsymbol{J}^T\right)^{\dagger}\boldsymbol{M}(\boldsymbol{x})\left(\boldsymbol{M}^{-1}(\boldsymbol{x})\left(\boldsymbol{C}(\boldsymbol{x},\dot{\boldsymbol{x}})\dot{\boldsymbol{x}} + \boldsymbol{G}(\boldsymbol{x}) + \hat{\boldsymbol{T}}_d\right)\right) \\ &\quad +\left(\boldsymbol{J}^T\right)^{\dagger}\boldsymbol{M}(\boldsymbol{x})\left(-\ddot{\boldsymbol{x}}_{\mathrm{d}} + \boldsymbol{K}_1 sign(\boldsymbol{S}) + \boldsymbol{K}_2\boldsymbol{S}^{\frac{m_n}{n}}\right).\end{aligned} \tag{17}$$

where $(\cdot)^{\dagger}$ denotes the pseudoinverse of $(\cdot)$. The vector $\boldsymbol{S}$ in (17) is chosen as:

$$\boldsymbol{S} = \boldsymbol{e} + \boldsymbol{\alpha} sign^{\gamma_1}\boldsymbol{e} + \boldsymbol{\beta} sign^{\gamma_2}\dot{\boldsymbol{e}}, \quad 1 < \gamma_2 < 2, \gamma_1 > \gamma_2 \tag{18}$$

The gain matrixes $\boldsymbol{\alpha}$, $\boldsymbol{\beta}$, $\boldsymbol{K}_1$, $\boldsymbol{K}_2$, and other variables in (17) and (18) are detailed in "Supplementary Material 1.pdf". The selected Lyapunov function takes the following form:

$$V = \frac{1}{2}\boldsymbol{S}^T\boldsymbol{S}. \tag{19}$$

Lemma 2: There exist some control parameters $\boldsymbol{\alpha}$, $\boldsymbol{\beta}$, $\boldsymbol{K}_1$, $\boldsymbol{K}_2$, γ_1, γ_2, m_n, n, g, h, p, and q such that:

$$\lim_{t\to\infty}V(t) = 0 \tag{20}$$

If $\dot{e}_i^{\gamma_2-1} \neq 0$ (i = 1,…,6), there exists a positive scalar Γ such that:

$$\dot{V} \le -\Gamma < 0. \tag{21}$$

Proof: The proof of *Lemma 2* is placed in the supplementary PDF file ("Supplementary Material 1.pdf").

Lemma 3: Assuming that the state of the system reaches the sliding surface at t_0, the tracking error $\boldsymbol{e}$ will converge to zero at time point t_e:

$$t_e \le \frac{e_i(t_0)^{1-1/\gamma_2}\beta_i^{1/\gamma_2}}{1-1/\gamma_2} + t_0, \ i = 1,2,...,6. \tag{22}$$

Proof: The proof of *Lemma 3* is placed in the supplementary PDF file ("Supplementary Material 1.pdf").

One important aspect to note is that the cable force vector $\boldsymbol{u}$ obtained in (17) consists of a sign function, leading to oscillations near the sliding surface. However, these oscillations are undesirable in practical experiments. To mitigate this issue, the sign function can be replaced with a hyperbolic tangent function, which effectively eliminates the oscillations but at the cost of the strong robustness of the sliding mode controller.

To maintain the stability of the tracking controller without sacrificing it, the sign function can be placed in the first derivative of the control input. Through further integration, the updated control input will avoid a sudden and abrupt jump caused by the sign function term. Let $\bar{\boldsymbol{u}} = \boldsymbol{M}^{-1}(\boldsymbol{x})\left(-\boldsymbol{J}^T\boldsymbol{u}\right)$, $\boldsymbol{u}_v = \dot{\bar{\boldsymbol{u}}}$, and $\boldsymbol{f}(\boldsymbol{x}) = \boldsymbol{M}^{-1}(\boldsymbol{x})\left(-\boldsymbol{C}(\boldsymbol{x},\dot{\boldsymbol{x}})\dot{\boldsymbol{x}} - \boldsymbol{G}(\boldsymbol{x}) - \hat{\boldsymbol{T}}_d\right)$, where $\bar{\boldsymbol{u}}$ is the updated control input.

Let $\boldsymbol{x}_1 = \boldsymbol{x}$ and $\boldsymbol{x}_2 = \dot{\boldsymbol{x}}$, we obtain:

$$\begin{cases} \boldsymbol{e} = \boldsymbol{x}_1 - \boldsymbol{x}_d \\ \dot{\boldsymbol{e}} = \boldsymbol{x}_2 - \dot{\boldsymbol{x}}_d \\ \ddot{\boldsymbol{e}} = \bar{\boldsymbol{u}} + \boldsymbol{f}(\boldsymbol{x}_1) - \ddot{\boldsymbol{x}}_d \\ \dddot{\boldsymbol{e}} = \boldsymbol{u}_v + \dot{\boldsymbol{f}}(\boldsymbol{x}_1) - \dddot{\boldsymbol{x}}_d \end{cases}. \tag{23}$$

The new sliding surface takes the following form:

$$\bar{\boldsymbol{S}} = \bar{\boldsymbol{\alpha}}\dot{\boldsymbol{e}} + \ddot{\boldsymbol{e}} + \bar{\boldsymbol{\beta}}\boldsymbol{S}. \tag{24}$$

where $\bar{\boldsymbol{\alpha}} = \mathrm{diag}([\bar\alpha_1,...,\bar\alpha_6])$ and $\bar{\boldsymbol{\beta}} = \mathrm{diag}([\bar\beta_1,...,\bar\beta_6])$, which contain positive elements.

After choosing $\bar V = \bar{\boldsymbol{S}}^T\bar{\boldsymbol{S}}/2$ as the Lyapunov function and calculating the derivative, we obtain:

$$\dot{\bar V} = \bar{\boldsymbol{S}}^T\dot{\bar{\boldsymbol{S}}} = \sum_{i=1}^{6}\bar S_i\dot{\bar S}_i. \tag{25}$$

where $\bar S_i$ is the i-th element of $\bar{\boldsymbol{S}}$ in (24), which is expressed by:

$$\bar S_i = \bar\alpha_i\dot e_i + \ddot e_i + \bar\beta_i S_i,\ i = 1,2,...,6. \tag{26}$$

Substituting (26) into (25) yields:

$$\begin{aligned} \bar S_i\dot{\bar S}_i &= \bar S_i\left(\bar\alpha_i\ddot e_i + \dddot e_i + \bar\beta_i\dot e_i + \bar\beta_i\gamma_1\alpha_i e_i^{\gamma_1-1}\dot e_i + \bar\beta_i\gamma_2\beta_i\dot e_i^{\gamma_2-1}\ddot e_i\right) \\ &= \bar S_i\Big(\bar\alpha_i\left(\bar u_i + f(\boldsymbol{x}_1)_i - \ddot x_{di}\right) + u_{vi} + \dot f(\boldsymbol{x}_1)_i - \dddot x_{di} \\ &\quad + \bar\beta_i\left(x_{2i} - \dot x_{di}\right) + \bar\beta_i\gamma_1\alpha_i\left(x_{1i} - x_{di}\right)^{\gamma_1-1}\left(x_{2i} - \dot x_{di}\right) \\ &\quad + \bar\beta_i\gamma_2\beta_i\left(x_{2i} - \dot x_{di}\right)^{\gamma_2-1}\left(\bar u_i + f(\boldsymbol{x}_1)_i - \ddot x_{di}\right)\Big). \end{aligned} \tag{27}$$

Let $\Lambda_{1i} = \bar\beta_i\gamma_1\alpha_i\left(x_{1i} - x_{di}\right)^{\gamma_1-1}$ and $\Lambda_{2i} = \bar\beta_i\gamma_2\beta_i\left(x_{2i} - \dot x_{di}\right)^{\gamma_2-1}$. Since Λ_{1i} and Λ_{2i} are positive scalars, equation (27) becomes:

$$\begin{aligned} \bar S_i\dot{\bar S}_i &= \bar S_i\Big(u_{vi} + \left(\bar\beta_i + \Lambda_{1i}\right)x_{2i} - \dddot x_{di} - \left(\bar\alpha_i + \Lambda_{2i}\right)\ddot x_{di} \\ &\quad - \left(\bar\beta_i + \Lambda_{1i}\right)\dot x_{di} + \left(\bar\alpha_i + \Lambda_{2i}\right)\bar u_i \\ &\quad + \left(\bar\alpha_i + \Lambda_{2i}\right)f(\boldsymbol{x}_1)_i + \dot f(\boldsymbol{x}_1)_i\Big). \end{aligned} \tag{28}$$

Then, the derivative ($\boldsymbol{u}_v$) of the updated control input $\bar{\boldsymbol{u}}$ can take the following form:

$$\begin{aligned} u_{vi} &= -\left(\bar\beta_i + \Lambda_{1i}\right)x_{2i} - \left(\bar\alpha_i + \Lambda_{2i}\right)\bar u_i - \left(\bar\alpha_i + \Lambda_{2i}\right)f(\boldsymbol{x}_1)_i \\ &\quad + \left(\bar\beta_i + \Lambda_{1i}\right)\dot x_{di} + \left(\bar\alpha_i + \Lambda_{2i}\right)\ddot x_{di} + \dddot x_{di} + \bar u_{vi}. \end{aligned} \tag{29}$$

Let a positive scalar $\bar\varepsilon_i$ satisfy $\left|\dot f(\boldsymbol{x}_1)_i\right| \le \bar\varepsilon_i$. Substituting (29) into (28) yields:

$$\bar S_i\dot{\bar S}_i = \bar S_i\left(\bar u_{vi} + \dot f(\boldsymbol{x}_1)_i\right) \le \bar S_i\bar u_{vi} + \left|\bar S_i\right|\bar\varepsilon_i. \tag{30}$$

Let $\bar u_{vi} = -\bar\rho_i sign\left(\bar S_i\right)$ and $\bar\rho_i = \bar\varepsilon_i + \bar\gamma_i, \bar\gamma_i > 0$. Equation (30) can be rewritten as:

$$\bar S_i\dot{\bar S}_i \le \left|\bar S_i\right|\left(-\bar\rho_i + \bar\varepsilon_i\right) \le -\left|\bar S_i\right|\bar\gamma_i < 0. \tag{31}$$

Eventually, the updated control input could be obtained:

$$\bar u_i = \int_0^t u_{vi}\,dt. \tag{32}$$

where

$$\begin{aligned} u_{vi} &= -\bar\rho_i sign\left(\bar S_i\right) - \left(\bar\beta_i + \Lambda_{1i}\right)x_{2i} - \left(\bar\alpha_i + \Lambda_{2i}\right)\bar u_i \\ &\quad - \left(\bar\alpha_i + \Lambda_{2i}\right)f(\boldsymbol{x}_1)_i + \left(\bar\beta_i + \Lambda_{1i}\right)\dot x_{di} + \left(\bar\alpha_i + \Lambda_{2i}\right)\ddot x_{di} + \dddot x_{di} \end{aligned} \tag{33}$$

C. Force Redistribution

Although the output of the auxiliary tracking control in (17) or (33) can maintain system stability in simulations, it does not guarantee that cable forces will always be positive in actual experiments. To ensure that the eventual cable forces $\boldsymbol{u}_s$ satisfy the specified constraints without compromising the tracking control performance, a force redistribution process is introduced to replace the original vectors $\boldsymbol{u}$ or $\bar{\boldsymbol{u}}$ with $\boldsymbol{u}_s$:

$$\boldsymbol{M}(\boldsymbol{x})\ddot{\boldsymbol{x}} + \boldsymbol{C}(\boldsymbol{x},\dot{\boldsymbol{x}})\dot{\boldsymbol{x}} + \boldsymbol{G}(\boldsymbol{x}) + \boldsymbol{T}_d = -\boldsymbol{J}^T\boldsymbol{u} = -\boldsymbol{J}^T\boldsymbol{u}_s. \tag{34}$$

where $\boldsymbol{u}_s = [u_{s1}, u_{s2}, \ldots, u_{sm}]^T$ satisfies $0 < u_{min} \le u_{si} \le u_{max}$. u_{min} and u_{max} denote minimum and maximum limits for cable forces. $\boldsymbol{u}_s$ also can minimize the given object function: $T(u_{s1}, u_{s2}, \ldots, u_{sm})$. When the goal is to minimize the Euclidean norm of cable forces, then $T(u_{s1}, u_{s2}, \ldots, u_{sm}) = \sqrt{u_{s1}^{\ 2} + u_{s2}^{\ 2} + \ldots + u_{sm}^{\ 2}}$.

Firstly, the Lagrangian function $L(\boldsymbol{u}_s, \boldsymbol{\eta}, \boldsymbol{v})$ is constructed as follows:

$$L\left(\boldsymbol{u}_s, \boldsymbol{\eta}, \boldsymbol{v}\right) = T\left(\boldsymbol{u}_s\right) - \sum_{i=1}^{6}\eta_i E_{qi}\left(\boldsymbol{u}_s\right) - \sum_{i=1}^{2m}\nu_i N_{ei}\left(\boldsymbol{u}_s\right). \tag{35}$$

where $\boldsymbol{E}_q = -\boldsymbol{J}^T\boldsymbol{u}_s + \boldsymbol{J}^T\boldsymbol{u} = [E_{q1}, E_{q2}, \ldots, E_{q6}]^T$, $\boldsymbol{N}_e = [N_{e1}, N_{e2}, \ldots, N_{e2m}]^T = [u_{s1} - u_{min}, -u_{s1} + u_{max}, u_{s2} - u_{min}, -u_{s2} + u_{max}, \ldots, u_{sm} - u_{min}, -u_{sm} + u_{max}]^T$, $\boldsymbol{\eta} = [\eta_1, \eta_2, ..., \eta_6]^T$, and $\boldsymbol{v} = [\nu_1, \nu_2, ..., \nu_{2m}]^T$.

Then, we utilize the Karush-Kuhn-Tucker conditions and (35) to formulate the optimization problem [36]:

$$\begin{aligned} \min\ & \frac{1}{2}\boldsymbol{d}^T\boldsymbol{B}_k\boldsymbol{d} + \nabla T\left(\boldsymbol{u}_{sk}\right)^T\boldsymbol{d} \\ s.t.\ & \boldsymbol{E}_q\left(\boldsymbol{u}_{sk}\right) + \nabla\boldsymbol{E}_q\left(\boldsymbol{u}_{sk}\right)\boldsymbol{d} = \boldsymbol{0}_{6\times1} \\ & \boldsymbol{N}_e\left(\boldsymbol{u}_{sk}\right) + \nabla\boldsymbol{N}_e\left(\boldsymbol{u}_{sk}\right)\boldsymbol{d} \ge \boldsymbol{0}_{2m\times1} \end{aligned} \tag{36}$$

where $\boldsymbol{d} \in \mathbb{R}^m$ is the gradient descent direction for $\boldsymbol{u}_s$. Equation (36) is solved in two steps using the smooth Newton's method. First, obtaining the correct gradient descent direction $\Delta\boldsymbol{z}_j$. Second, obtaining the update increment $\rho_{z1}^{\varsigma_z}$. Similar to this process, after obtaining the gradient descent direction $\boldsymbol{d} \in \mathbb{R}^m$, the update increment ρ_1^{ς} for $\boldsymbol{u}_s$ can be solved by the selected merit function (78). Equations (72)-(86) and the definition of variables are placed in the supplementary PDF file ("Supplementary Material 1.pdf"). Kindly refer to it for further information.

TABLE I lists a complete solving process for calculating cable forces within specified upper and lower limits. The objective function is not confined to the commonly used Euclidean norm function and can adopt other specified functions. The process of force redistribution directly converts the unconstrained cable forces (produced by the auxiliary tracking control) into new cable forces $\boldsymbol{u}_s$ that satisfy the constraints. The redistribution principle in (34) ensures that the new cable forces do not affect the tracking performance. Such a feature allows for the seamless integration of the cable force redistribution with the auxiliary tracking control.

TABLE I
FORCE REDISTRIBUTION SOLVING PROCESS

Input: Original vector $\boldsymbol{u}$ from (17) or vector $\bar{\boldsymbol{u}}$ from (32) and (33)
Output: Optimized cable forces $\boldsymbol{u}_s$
Initialize Parameters:
    Set $\boldsymbol{E}_q(\boldsymbol{u}_s)$, $N_e(\boldsymbol{u}_s)$, $\boldsymbol{u}_{s0}, \boldsymbol{\eta}_0, \boldsymbol{v}_0, \boldsymbol{B}_0$, and $\boldsymbol{d}_0$
    Define object function $T(u_{s1}, u_{s2}, \ldots, u_{sm})$
    Define Lagrangian function $L(\boldsymbol{u}_s, \boldsymbol{\eta}, \boldsymbol{v})$ using (35)
    Set $\rho_1, \rho_2, \rho_{z1}, \rho_{z2}, \varepsilon_0, \varepsilon_1, \varepsilon_2, \varepsilon_3, \varepsilon_{z0}, \gamma, \delta, \sigma_0, \vartheta$, and $k = 0$
while condition (82) is unsatisfied **and** $k \le 3000$ **do**
    Set z_0, $\boldsymbol{\varpi}$, and $j = 0$
    while $\|\boldsymbol{H}(z_j)\| > \varepsilon_3$ **and** $j \le 150$ **do**
        Obtain Δz_j from (72)
        Obtain ς_z from (77)
        Update z using $z_{j+1} = z_j + \rho_{z1}^{\varsigma_z}\Delta z_j$
    end while
    if $\|\boldsymbol{H}(z_j)\| \le \varepsilon_3$ **or** $j == 150$ **then**
        $\boldsymbol{d}_k = \boldsymbol{d}_j$, $\boldsymbol{\eta}_{zk} = \boldsymbol{\eta}_{zj}$, $\boldsymbol{v}_{zk} = \boldsymbol{v}_{zj}$
    end if
    Obtain ς from (80) and (81)
    Update $\boldsymbol{u}_s$ using $\boldsymbol{u}_{sk+1} = \boldsymbol{u}_{sk} + \rho_1^{\varsigma}\boldsymbol{d}_k$
    if condition (82) is satisfied **then**
        Output $\boldsymbol{u}_s$ and **break while**
    else
        Update $\boldsymbol{\eta}_{k+1}$, $\boldsymbol{v}_{k+1}$, and $\boldsymbol{B}_{k+1}$
    end if
end while
if condition (82) is satisfied or $k == 3000$ **then**
    Output $\boldsymbol{u}_s$
end if

V. EXPERIMENT IMPLEMENTATION

To validate the effectiveness of the designed trajectory tracking control and the cable force redistribution process, this section conducts experimental tests on two different configurations of the robot. Fig. 6 illustrates the experimental setup. Here, a Leica Laser Tracker (AT901-MR) is used to measure and record the position of the robot.

The system utilizes motor drives in speed control mode to achieve the motion control of the CDR (see Fig. 5). The linear velocity ($\dot{l}_i$) of each cable is calculated by the CDR's inverse model and converted into the motor's angular velocity ($w_{d,i}$) based on drum radius ($r_{\text{drum}} = 25$ mm). The motor position and speed ($w_{\text{real},i}$) feedback from the drive are used to calculate the robot's position. A PI controller processes the error between target cable forces ($\boldsymbol{u}_\text{s}$) and actual cable forces ($\boldsymbol{u}_{\text{actual}}$), whose output is then integrated with the motor's speed control signal.

To demonstrate the importance of the force redistribution during trajectory tracking of the robot, we provide an example comparing the differences between cable forces generated by the auxiliary tracking control and those generated by the force redistribution process. Fig. 7(a) illustrates the cable forces and motion trajectories under the auxiliary tracking control. Fig. 7(b) shows the cable forces and motion trajectories under a combination of the auxiliary tracking control and the force redistribution process. In Fig. 7(a), the cable forces of Cables 3 and 4 are negative, indicating that these two cables need to exert reverse pressure. However, in practice, cables can only exert tension, not pressure. Therefore, if we rely solely on the auxiliary tracking control in experiments, Cables 3 and 4 will become slack, and the robot may fail to achieve the expected trajectory tracking. After force redistribution, as shown in Fig. 7(b), the forces of four cables are positive. In Fig. 7(a) and Fig. 7(b), the obtained trajectories closely match the designed ones, with errors approaching zero. The obtained trajectories remain unchanged before and after force redistribution. The overlap of the curves in Fig. 7(c) and Fig. 7(d) indicates that the control input $\boldsymbol{u}_{real}$ is not affected by the force redistribution.

Next, we will analyze why the force redistribution does not affect trajectory tracking performance and the stability of the control system. According to (5), $\boldsymbol{u}$ is a 4×1 cable force vector, while the left side of the equation ultimately results in a 3×1 vector. The difference in dimensions arises because cables can only exert tension and not pressure, necessitating that the

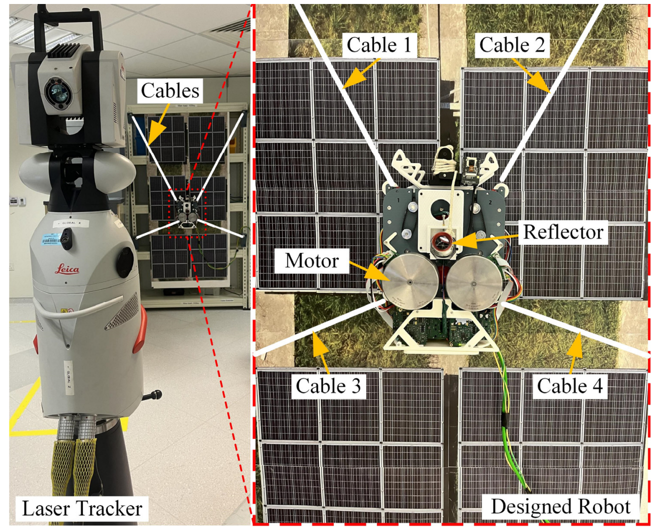

Fig. 6. Experimental setup.

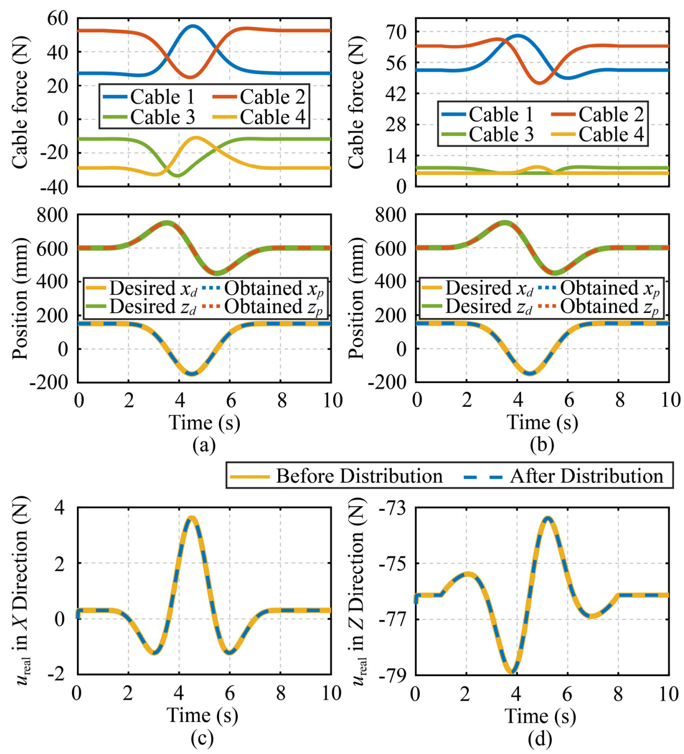

Fig. 7. Performance comparison before and after force redistribution.

number of cables exceeds the number of controllable degrees of freedom by one. This characteristic of redundant actuation means that for the same motion state of the robot, there are multiple solutions for the cable force vector $\boldsymbol{u}$. This is the foundation of force redistribution.

In (5), using the Jacobian matrix $\boldsymbol{J}$, the cable force vector $\boldsymbol{u}$ is transformed into a 3×1 vector, which we denote as $\boldsymbol{u}_{\text{real}}$, as shown in (37). In the stability proof process, we essentially use $\boldsymbol{u}_{\text{real}}$ for verification because the right side of the dynamic model (5) consistently includes the Jacobian matrix $\boldsymbol{J}$ that transforms the cable force vector $\boldsymbol{u}$ into $\boldsymbol{u}_{\text{real}}$. Thus, in the stability proof, the control input is always in the form of $\boldsymbol{u}_{\text{real}}$. Note that $\boldsymbol{u}_{\text{real}}$ is a 3×1 vector linked to the 4×1 vector $\boldsymbol{u}$ through the Jacobian matrix $\boldsymbol{J}$. As previously analyzed, for the same $\boldsymbol{u}_{\text{real}}$, multiple different vectors $\boldsymbol{u}$ can be solved. The principle of force redistribution lies in selecting a vector $\boldsymbol{u}$ that satisfies the given constraints from these different cable force vectors. Although these vectors differ, they all can be transformed into the same $\boldsymbol{u}_{\text{real}}$ through the Jacobian matrix $\boldsymbol{J}$. Therefore, the value of $\boldsymbol{u}_{\text{real}}$ essentially remains unchanged, ensuring that the system stability and trajectory tracking performance are not affected.

$$\begin{cases} \boldsymbol{M}(\boldsymbol{x})\ddot{\boldsymbol{x}}+\boldsymbol{C}(\boldsymbol{x},\dot{\boldsymbol{x}})\dot{\boldsymbol{x}}+\boldsymbol{G}(\boldsymbol{x})+\boldsymbol{T}_d = -\boldsymbol{J}^T\boldsymbol{u} \\ \boldsymbol{M}(\boldsymbol{x})\ddot{\boldsymbol{x}}+\boldsymbol{C}(\boldsymbol{x},\dot{\boldsymbol{x}})\dot{\boldsymbol{x}}+\boldsymbol{G}(\boldsymbol{x})+\boldsymbol{T}_d = \boldsymbol{u}_{\text{real}} \\ \boldsymbol{u}_{\text{real}} = -\boldsymbol{J}^T\boldsymbol{u} \end{cases} \tag{37}$$

In the experiment, we validated the robot's adjustable compliance in response to external disturbances through two different configurations. Low compliance indicates that the robot has strong resistance to external disturbances, with increased cable forces enhancing its position-holding capability. High compliance, on the other hand, indicates that the robot has lower resistance to external disturbances, resulting in significant displacement in the direction of the disturbances. This allows the robot to avoid excessive cable forces by sacrificing some trajectory tracking accuracy, which helps to reduce the risk of cable breakage and ensures the safe operation of the robot.

The initial parameters in the force redistribution process are: $\boldsymbol{u}_{s0}=[30, 30, 5, 5]^T$, $\boldsymbol{\eta}_0=[0, 0, 0]^T$, $\boldsymbol{v}_0=[0, 0, 0, 0, 0, 0, 0, 0]^T$, $\rho_1=0.5$, $\rho_2=0.1$, $\boldsymbol{B}_0=\text{diag}([1, 1, 1, 1])$, $\delta=0.05$, $\sigma_0=0.8$, $\varepsilon_1=10^{-6}$, $\varepsilon_2=10^{-5}$, $\varepsilon_3=10^{-6}$, $\rho_{z1}=0.5$, $\rho_{z2}=0.2$, $\varepsilon_0=0.05$, $\vartheta=0.05$, $\varepsilon_{z0}=0.05$, $\gamma=0.05$, $\boldsymbol{d}_0=[1, 1, 1, 1]^T$, $\boldsymbol{\eta}_{z0}=[0, 0, 0]^T$, $\boldsymbol{v}_{z0}=[0, 0, 0, 0, 0, 0, 0, 0]^T$. The control parameters are: $\boldsymbol{\alpha}=\text{diag}([5, 5, 5])$, $\boldsymbol{\beta}=\text{diag}([1.5, 1.5, 1.5])$, $\overline{\boldsymbol{\alpha}}=\text{diag}([15000, 17000, 12])$, $\overline{\boldsymbol{\beta}}=\text{diag}([12000, 15000, 10])$, $\boldsymbol{\beta}_1=\text{diag}([10, 10, 10])$, $\boldsymbol{\beta}_2=\text{diag}([150, 150, 150])$, $\overline{\varepsilon}_1=0.1$, $\overline{\varepsilon}_2=0.001$, $\overline{\varepsilon}_3=0.001$, $\overline{\gamma}_1=0.1$, $\overline{\gamma}_2=0.001$, $\overline{\gamma}_3=0.01$, $\gamma_1=7/3$, $\gamma_2=5/3$. The control cycle of the Beckhoff controller is 1 ms.

A. Configuration 1

Configuration 1 of the robot is depicted in Fig. 4(a). The coordinates of four anchor points are specified as follows: A_1 (-549.5, 1220), A_2 (549.5, 1220), A_3 (-549.5, 0), and A_4 (549.5, 0). The coordinates of four anchor points located at the robot are: B_1 (-100, 100), B_2 (100, 100), B_3 (-100, -100), and B_4 (100, -100). The robot's trajectories include circular (in Fig. 8) and rectangular (in Fig. 10) shapes. For each type of the trajectories, we set up four scenarios (Scenario 1 - Scenario 4).

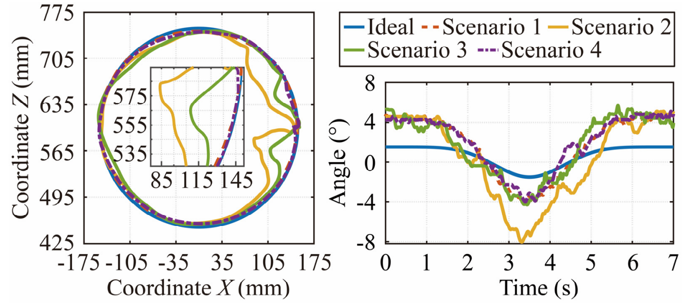

Fig. 8. Circular trajectories and Euler angles in Configuration 1.

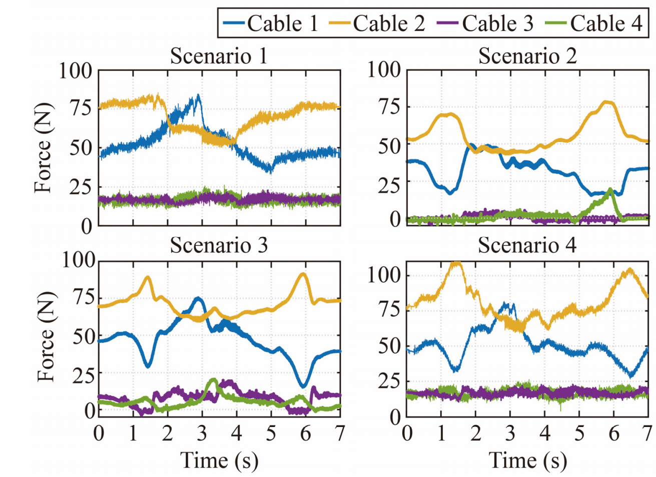

Fig. 9. Four cable forces corresponding to four scenarios in Fig. 8.

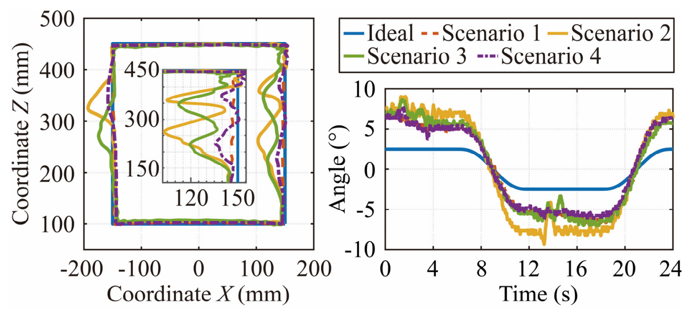

Fig. 10. Rectangular trajectories and Euler angles in Configuration 1.

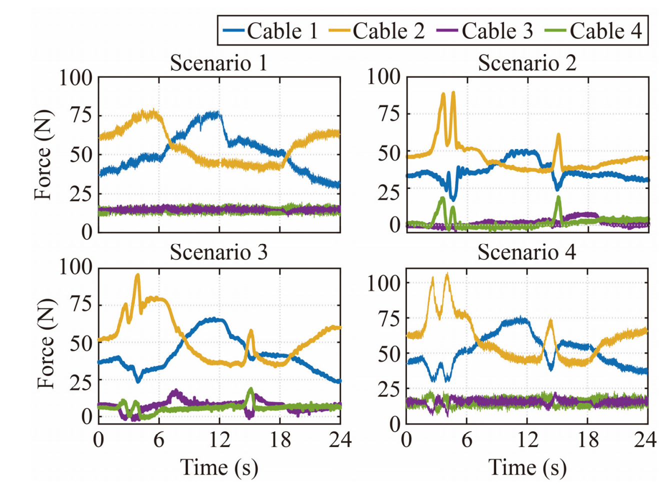

Fig. 11. Four cable forces corresponding to four scenarios in Fig. 10.

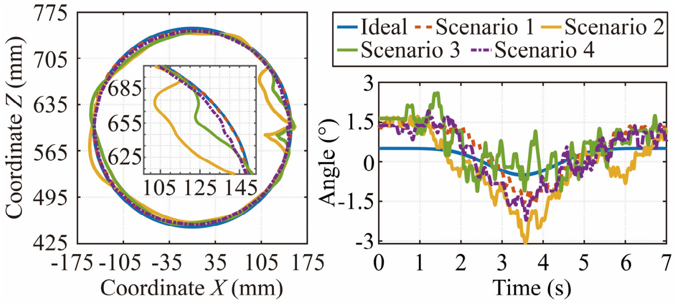

Fig. 12. Circular trajectories and Euler angles in Configuration 2.

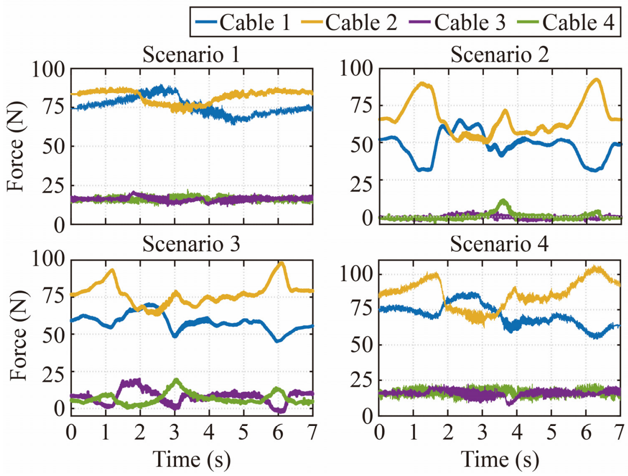

Fig. 13. Four cable forces corresponding to four scenarios in Fig. 12.

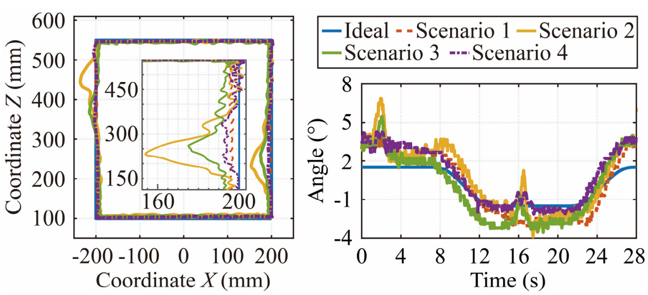

Fig. 14. Rectangular trajectories and Euler angles in Configuration 2.

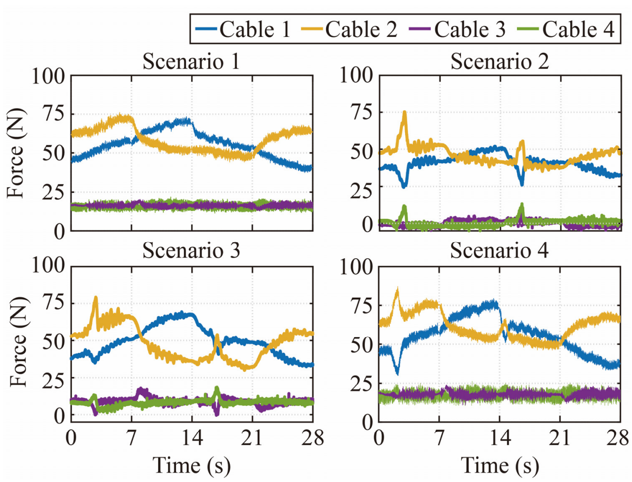

Fig. 15. Four cable forces corresponding to four scenarios in Fig. 14.

Scenario 1 employs the designed auxiliary tracking control and force redistribution process without external disturbances, with control parameters set to $u_{\min} = 15$ and $u_{\max} = 120$.

TABLE II
TRACKING ERRORS IN FIG. 8

		Scenario 1	Scenario 2	Scenario 3	Scenario 4
X	Max.	2.92 mm	65.90 mm	39.52 mm	9.19 mm
	RMSE	1.13 mm	26.30 mm	12.40 mm	4.30 mm
Z	Max.	4.61 mm	15.95 mm	12.45 mm	7.97 mm
	RMSE	2.53 mm	7.99 mm	5.38 mm	4.50 mm
β	Max.	3.38°	6.61°	4.69°	3.61°
	RMSE	2.27°	3.11°	2.86°	2.33°

TABLE III
TRACKING ERRORS IN FIG. 10

		Scenario 1	Scenario 2	Scenario 3	Scenario 4
X	Max.	5.58 mm	46.96 mm	37.75 mm	14.32 mm
	RMSE	2.86 mm	12.03 mm	10.64 mm	5.55 mm
Z	Max.	3.86 mm	24.08 mm	9.51 mm	5.30 mm
	RMSE	2.12 mm	6.17 mm	4.84 mm	2.52 mm
β	Max.	4.48°	6.84°	6.17°	5.13°
	RMSE	2.92°	4.33°	3.19°	2.76°

TABLE IV
TRACKING ERRORS IN FIG. 12

		Scenario 1	Scenario 2	Scenario 3	Scenario 4
X	Max.	2.88 mm	38.82 mm	20.66 mm	4.79 mm
	RMSE	1.21 mm	13.96 mm	7.42 mm	2.06 mm
Z	Max.	4.26 mm	12.63 mm	11.36 mm	4.81 mm
	RMSE	2.29 mm	5.48 mm	4.68 mm	2.59 mm
β	Max.	1.13°	2.58°	2.14°	1.99°
	RMSE	0.70°	0.95°	0.80°	0.75°

TABLE V
TRACKING ERRORS IN FIG. 14

		Scenario 1	Scenario 2	Scenario 3	Scenario 4
X	Max.	4.98 mm	46.05 mm	24.98 mm	11.59 mm
	RMSE	2.93 mm	10.19 mm	8.53 mm	4.64 mm
Z	Max.	3.69 mm	11.93 mm	11.49 mm	5.72 mm
	RMSE	1.92 mm	6.19 mm	5.58 mm	2.98 mm
β	Max.	2.61°	5.35°	3.95°	2.84°
	RMSE	1.14°	1.52°	1.32°	1.23°

Scenarios 2 to 4 include disturbances, with the parameters set as follows: Scenario 2 has $u_{\min} = 0$ and $u_{\max} = 120$, Scenario 3 has $u_{\min} = 6$ and $u_{\max} = 120$, and Scenario 4 has $u_{\min} = 15$ and $u_{\max} = 120$. The purpose of comparing these scenarios is to evaluate the effectiveness of the designed controller under different conditions and to validate its compliance when facing external disturbances.

Fig. 8 illustrates the tracking effect of position and Euler angles under four different scenarios in Configuration 1. Fig. 9 depicts the cable forces corresponding to the circular trajectories in Fig. 8. Table II lists the root mean square error (RMSE) and the maximum tracking error in these scenarios. Without disturbances, the maximum angular error is 3.38°. With external disturbances, as the robot's compliance decreases, the angular error gradually reduces from 6.61° to 3.61°. In Scenario 1, after force redistribution, the minimum cable force is approximately 15 N in the absence of disturbances. The maximum position error is 4.61 mm, occurring in the Z-axis direction. In Scenarios 2 to 4, external disturbances are introduced during the robot's motion, which causes a position error of 65.9 mm along the X-axis. However, the tracking controller still maintains stable tracking. Despite the significant deviation, once the disturbances subside, the robot can quickly converge back to the predetermined trajectory. The controller exhibits high compliance to external disturbances, allowing the robot to deviate (65.9 mm) in the direction of the disturbances. By intentionally sacrificing tracking accuracy, the controller effectively mitigates a sudden increase in cable forces. As the robot's ability to resist external disturbances gradually improves, the position error decreases from 65.9 mm to 9.19 mm, but the maximum cable force increases from 78.2 N to 111.3 N.

Regarding the rectangular trajectory, Fig. 10 and Fig. 11 show the trajectory tracking performance and changes in cable force under four different scenarios. In the absence of any disturbances, the maximum position error remains within 5.58 mm while all cables maintain positive tension. From Scenario 2 to Scenario 4, it is observed that the robot's ability to resist disturbances improved, leading to a reduction in maximum position error from 46.96 mm to 14.32 mm. However, this improvement comes at the cost of reduced compliance, resulting in an increase in cable forces from 89.5 N to 107.3 N. TABLE III indicates that the maximum angular error and RMSE decrease as the robot's compliance decreases. Interestingly, the RMSE under disturbances (Scenario 4) is smaller than the RMSE without disturbances (Scenario 1). This occurs because, as the robot moves along the *Z*-axis, external disturbances inadvertently adjust the robot's angle, bringing it closer to the target angle. Throughout the process, the robot consistently maintains its ability to track the predetermined trajectory, even when the position error reaches a maximum of 46.96 mm.

B. Configuration 2

Configuration 2 of the robot is shown in Fig. 4(d). The coordinates of four anchor points are specified as follows: A_1 (-1159.5, 1747), A_2 (1159.5, 1747), A_3 (-1159.5, 0), and A_4 (1159.5, 0). The robot's trajectories include circular (Fig. 12) and rectangular (Fig. 14) shapes. The four scenarios in Configuration 2 are the same as those in Configuration 1. In Scenario 1, by comparing Tables II to V, it can be observed that Configuration 2 exhibits superior trajectory tracking performance (position and angle) compared to Configuration 1. This phenomenon occurs because Configuration 1 has a smaller workspace, where the trajectory is closer to the workspace boundary. In contrast, Configuration 2 has a larger workspace, with the trajectory being further from the workspace boundary.

In the circular trajectory depicted in Fig. 12, the maximum position error without disturbances is 4.26 mm, and the maximum angular error without disturbances is 1.13° (see TABLE IV). From Scenario 2 to Scenario 4, the maximum position error of the robot under external disturbances decreases from 38.82 mm to 4.81 mm, and the maximum angular error decreases from 2.58° to 1.99°. However, as a trade-off, the maximum cable force increases from 92.62 N to 106.2 N (see Fig. 13). In the rectangular trajectory shown in Fig. 14, the maximum position error without disturbances is 4.98 mm, and the maximum angular error is 2.61°. As the robot's ability to resist external disturbances gradually improves, the position error decreases from 46.05 mm to 11.59 mm, and the maximum angular error decreases from 5.35° to 2.84° (see TABLE V). However, the maximum cable force increases from 75.3 N to 86.1 N (see Fig. 15). Even when the position error reaches a deviation of 46.05 mm, the robot still maintains stable trajectory tracking, demonstrating the stability of the controller.

VI. CONCLUSION

This study developed a portable CDR with a compliant tracking controller that integrated auxiliary tracking control and cable force redistribution. Experimental results verified that the robot could effectively adjust its compliance in response to external disturbances. When operating at high compliance, the robot sacrifices tracking accuracy to mitigate the sudden increase in cable forces caused by disturbances. Conversely, the robot is better at resisting disturbances at low compliance to maintain accurate trajectory tracking. Moreover, experiments validated the controller's ability to converge and maintain stability, even with deviations up to 65.9 mm. Once the external disturbances cease, the controller continues to accurately track the predetermined trajectory. Additionally, the experimental results indicated that the force redistribution process efficiently redistributed the cable forces to meet the given constraints. The seamless integration of the force redistribution process with the auxiliary tracking control ensures the stability and compliance of the robot during trajectory tracking. Furthermore, the robot relies only on simple anchor points from the external environment, and its workspace can be quickly reconfigured as needed. Future work will explore applications in unstructured environments such as facade operations.

REFERENCES

[1] C. H. Lee, K. W. Gwak, "Design of a novel cable-driven parallel robot for 3D printing building construction," *Int. J. Adv. Manuf. Technol.*, vol. 123, no. 11, pp. 4353–4366, 2022.

[2] H. Sun, X. Tang, Z. Cui, *et al.*, "Dynamic response of spatial flexible structures subjected to controllable force based on cable-driven parallel robots," *IEEE/ASME Trans. Mechatron.*, vol. 25, no. 6, pp. 2801–2811, 2020.

[3] M. Seo, S. Yoo, M. Choi, *et al.*, "Vibration reduction of flexible rope-driven mobile robot for safe facade operation," *IEEE/ASME Trans. Mechatron.*, vol. 26, no. 4, pp. 1812–1819, 2021.

[4] Y. Shi, J. Wang, S. Li, *et al.*, "Tracking control of cable-driven planar robot based on discrete-time recurrent neural network with immediate discretization method," *IEEE Trans. Ind. Inform.*, vol. 19, no. 6, pp. 7414–7422, 2022.

[5] M. Ghanatian, M. R. H. Yazdi, M. T. Masouleh, "Experimental study on controlling suspended cable-driven parallel robots for autonomous video-capturing of football games and obtaining the statistics of the games," *Mechatronics*, vol. 95, pp. 103058, 2023.

[6] W. Shang, B. Zhang, B. Zhang, et al, "Synchronization control in the cable space for cable-driven parallel robots," *IEEE Trans. Ind. Electron.*, vol. 66, no. 6, pp. 4544–4554, Jun. 2019.

[7] H. Jia, W. Shang, F. Xie, *et al.*, "Second-order sliding-mode-based synchronization control of cable-driven parallel robots," *IEEE/ASME Trans. Mechatron.*, vol. 25, no. 1, pp. 383-394, 2019.

[8] M. H. Korayem, H. Tourajizadeh, M. Jalali, and E. Omidi, "Optimal path planning of spatial cable robot using optimal sliding mode control," *Int. J. Adv. Robotic Syst.*, vol. 9, no. 5, 2012, Art. no. 168.

[9] Y. Sugahara, T. Ueki, D. Matsuura, et al, "Offline Reference Trajectory Shaping for a Cable-Driven Earthquake Simulator Based on a

Viscoelastic Cable Model," *IEEE Robot. Autom. Lett.*, vol. 7, no. 2, pp. 2415–2422, 2022.
[10] Z. Shao, T. Li, X. Tang, *et al.*, "Research on the dynamic trajectory of spatial cable-suspended parallel manipulators with actuation redundancy," *Mechatronics*, vol. 49, pp. 26–35, 2018.
[11] G. Zuccon, A. Doria, M. Bottin, *et al.*, "Planar Model for Vibration Analysis of Cable Rehabilitation Robots," *Robotics*, vol. 11, no. 6, pp. 154, 2022.
[12] S. W. Hwang, D. H. Kim, J. Park, et al, "Equilibrium Configuration Analysis and Equilibrium-Based Trajectory Generation Method for Under-Constrained Cable-Driven Parallel Robot," *IEEE Access*., vol. 10, pp. 112134–112149, 2022.
[13] H. Jamshidifar, A. Khajepour, A. H. Korayem, "Wrench feasibility and workspace expansion of planar cable-driven parallel robots by a novel passive counterbalancing mechanism," *IEEE Trans. Robot.* vol. 37 no. 3, pp. 935–947, 2020.
[14] R. Wang, S. Li, Y. Li, "A suspended cable-driven parallel robot with articulated reconfigurable moving platform for Schönflies motions," *IEEE/ASME Trans. Mechatron.*, vol. 27, no. 6, pp. 5173–5184, 2022.
[15] M. A. Khosravi, H. D. Taghirad, "Robust PID control of fully-constrained cable driven parallel robots," *Mechatronics*, vol. 24, no. 2, pp. 87–97, 2014.
[16] R. Babaghasabha, M. A. Khosravi, and H. D. Taghirad, "Adaptive robust control of fully-constrained cable driven parallel robots," *Mechatronics*, vol. 25, no. 2, pp. 27–36, 2015.
[17] M. A. Khosravi and H. D. Taghirad, "Dynamic modeling and control of parallel robots with elastic cables: Singular perturbation approach," *IEEE Trans. Robot.*, vol. 30, no. 3, pp. 694–704, 2014.
[18] B. Zhang, W. Shang, S. Cong, *et al.*, "Dual-Loop Dynamic Control of Cable-Driven Parallel Robots Without Online Tension Distribution," *IEEE Trans. Syst. Man Cybern. Syst.*, vol. 52, no. 10, pp. 6555–6568, 2022.
[19] S. Kawamura, H. Kino, C. Won, "High-speed manipulation by using parallel wire-driven robots," *Robot.*, vol. 18, no. 1, pp. 13–21, 2000.
[20] H. Kino, T. Yahiro, S. Taniguchi, *et al.*, "Sensorless position control using feedforward internal force for completely restrained parallel-wire-driven systems," *IEEE Trans. Robot.*, vol. 25, no. 2, pp. 467–474, 2009.
[21] H. D. Taghirad, Y. B. Bedoustani, "An analytic-iterative redundancy resolution scheme for cable-driven redundant parallel manipulators," *IEEE Trans. Robot.*, vol. 27, no. 6, pp. 1137–1143, 2011.
[22] W. B. Lim, S. H. Yeo, G. Yang, "Optimization of tension distribution for cable-driven manipulators using tension-level index," *IEEE/ASME Trans. Mechatron.*, vol. 19, no. 2, pp. 676–683, 2013.
[23] M. Agahi, L. Notash, "Redundancy resolution of wire-actuated parallel manipulators," *Trans. Can. Soc. Mech. Eng.*, vol. 33, no. 4, pp. 561–573, 2009.
[24] S. R. Oh and S. K. Agrawal, "Cable suspended planar robots with redundant cables: Controllers with positive tensions," *IEEE Trans. Robot.*, 21, no. 3, pp. 457–465, 2005.
[25] A. Ameri, A. Molaei, M. A. Khosravi, *et al.*, "Control-Based Tension Distribution Scheme for Fully Constrained Cable-Driven Robots," *IEEE/ASME Trans. Mechatron.*, vol. 69, no. 11, pp. 11383–11393, 2021.
[26] Z. Cui, X. Tang, S. Hou, *et al.*, "Research on controllable stiffness of redundant cable-driven parallel robots," *IEEE/ASME Trans. Mechatron.*, vol. 23, no. 5, pp. 2390–2401, 2018.
[27] X. Geng, M. Li, Y. Liu, *et al.*, "Analytical tension-distribution computation for cable-driven parallel robots using hypersphere mapping algorithm," *Mech. Mach. Theory.*, vol. 145, pp. 103692, 2020.
[28] R. Qi, M. Rushton, A. Khajepour, and W. W. Melek, "Decoupled modeling and model predictive control of a hybrid cable-driven robot (HCDR)," *Robot. Auton. Syst.*, vol. 118, pp. 1–12, 2019.
[29] J. C. Santos, M. Gouttefarde, A. A. Chemori, "A Nonlinear model predictive control for the position tracking of cable-driven parallel robots," *IEEE Trans. Robot.*, vol. 38, no. 4, pp. 2597–2616, 2022.
[30] C. Sancak and M. Itik, "Out-of-plane vibration suppression and position control of a planar cable-driven robot," *IEEE/ASME Trans. Mechatron.*, vol. 27, no. 3, pp. 1311–1320, 2021.
[31] Y. Lu, C. Wu, W. Yao, *et al.*, "Deep Reinforcement Learning Control of Fully-Constrained Cable-Driven Parallel Robots," *IEEE Trans. Ind. Electron.*, vol. 70, no. 7, pp. 7194–7204, 2022.
[32] F. Xie, W. Shang, B. Zhang, et al, "High-precision trajectory tracking control of cable-driven parallel robots using robust synchronization," *IEEE Trans. Ind. Electron.*, vol. 17, no. 4, pp. 2488-2499, 2020.
[33] H. An, Y. Zhang, H. Yuan, *et al.*, "Design control and performance of a cable-driving module with external encoder and force sensor for cable-driven parallel robots," *J. Mech. Robot.*, vol. 14, no. 1, pp. 014502, 2022.
[34] R. C. Bonitz and T. C. Hsia, "Internal force-based impedance control for cooperating manipulators," *IEEE Trans. Robot. Autom.*, vol. 12, no. 1, pp. 78–89, 1996.
[35] A. R. Barroso, R. Saltaren, G. A. Portilla, *et al.*, "Cable-driven parallel robot with reconfigurable end effector controlled with a compliant actuator," *Sensors*, vol. 18, no. 9, pp. 2765, 2018.
[36] N. Jorge and J. W. Stephen, *Numerical optimization*. New York, NY, USA: Springer Science+Business Media, LLC, 2006, pp. 537.

Haining Sun (Member, IEEE) received the B.Eng. degree in mechanical engineering from Shandong University, Jinan, China, in 2017, and the Ph.D. degree in mechanical engineering from Tsinghua University, Beijing, China, in 2022. He is currently with the Singapore Institute of Manufacturing Technology, Singapore. His current research interests include vibration control, dynamic control, force control, and cable-driven robots.

Xiaoqiang Tang received the Ph.D. degree in mechanical engineering from Tsinghua University, Beijing, China, in 2001. He is currently a Professor with the Department of Mechanical Engineering, Tsinghua University. His research interests include parallel manipulators, robots, and reconfigurable manufacturing technology.

Shuzhi Sam Ge (Fellow, IEEE) received the B.Sc. degree from the Beijing University of Aeronautics and Astronautics, Beijing, China, in 1986, and the Ph.D. degree from the Imperial College London, London, U.K., in 1993.

He is a fellow of SAEng, IEEE, IFAC, IET and CAA, Professor with the Department of Electrical and Computer Engineering, PI Member of Institute for Functional Intelligent Materials, the National University of Singapore. Founder of Institute for Future (IFF), Qingdao University, China. He Serves as President Elect of Asian Control Association, 2022-2024, IFAC executive officers as Council Member, 2023-2026, Steering Committee Chair of International Conference on Social Robotics. He served as Vice President of Technical Activities and Membership Activities, 2009-2012, Member of Board of Governors, 2007-2009, and Chair of Technical Committee on Intelligent Control, 2005-2008, of IEEE Control Systems Society. He was the recipient of many award including National Technology Award from Singapore, IEEE Control Systems Society Distinguished Member Award, AI Grand Challenge Award from AI SG. His research interests include robotics, intelligent systems, and intelligent materials. He has (co)-authored nine books, and over 800 international journal and conference papers, with high H index (110) and citations (58,000).